Supplementary Materials for

Brain activity fluctuations propagate as waves traversing the cortical hierarchy

Yameng Gu, Lucas E. Sainburg, Sizhe Kuang, Feng Han, Jack W. Williams, Yikang Liu, Nanyin Zhang, Xiang Zhang, David A. Leopold, Xiao Liu.

Correspondence to: xxl213@psu.edu.

This file includes:

Figs. S1 to S29.

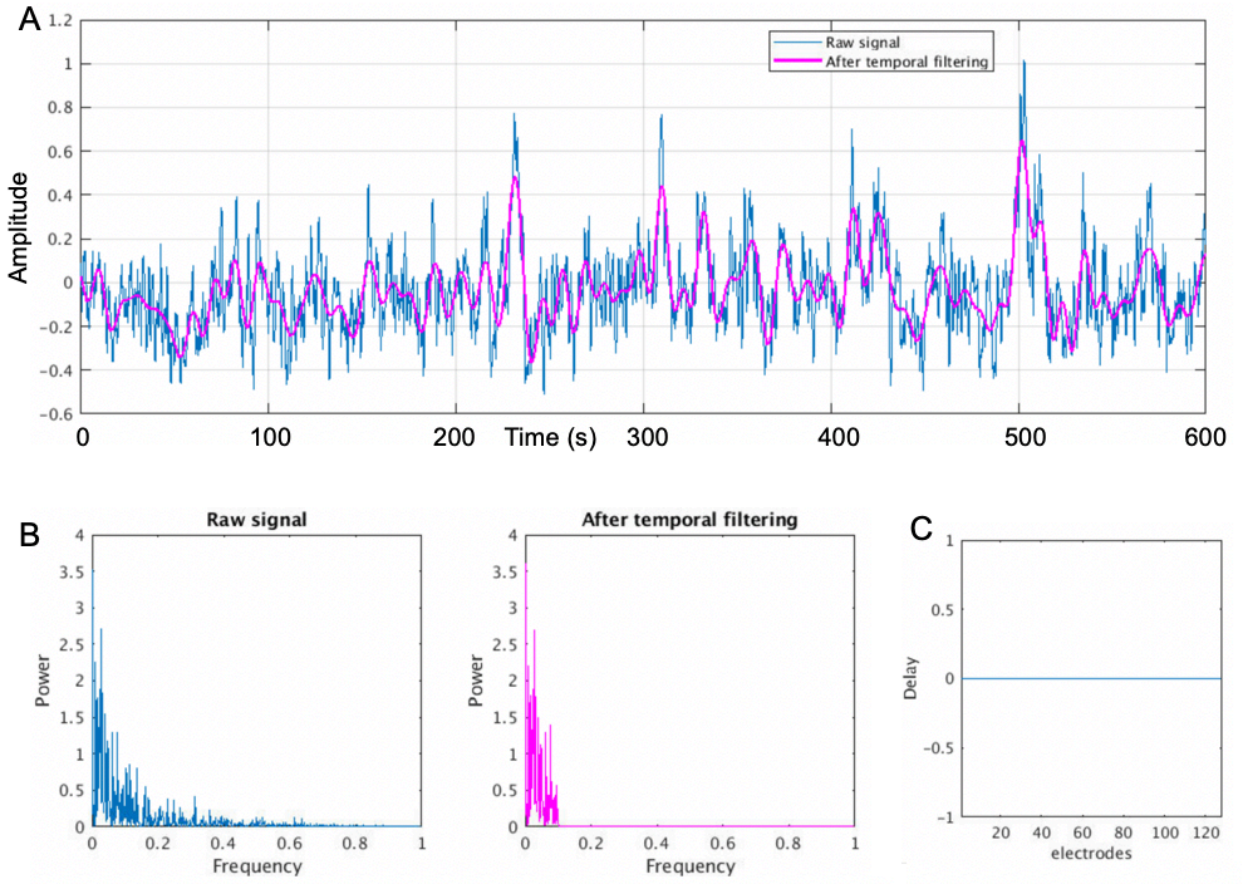

Fig. S1.
The performance of the temporal filtering used in the analyses. (A) An example time series of the gamma-band power of monkey ECoG signal (blue) and its temporally filtered (<0.1 Hz) version. (B) The power spectrum of the gamma power signal and the filtered signal. (C) The phase delay between the unfiltered and filtered signals at each electrode.

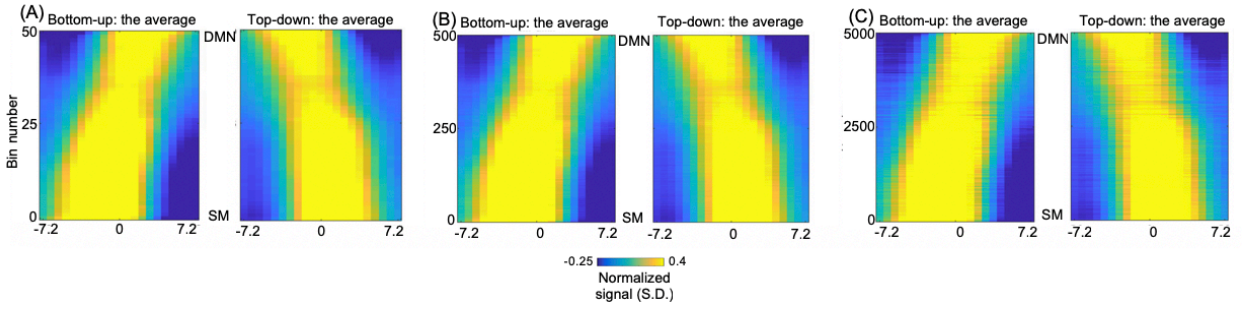

Fig. S2.
The bottom-up and top-down propagations on the time-position plot in Fig. 2E were examined at different number of position bins, e.g., 50 (A), 500 (B), 5000 (C).

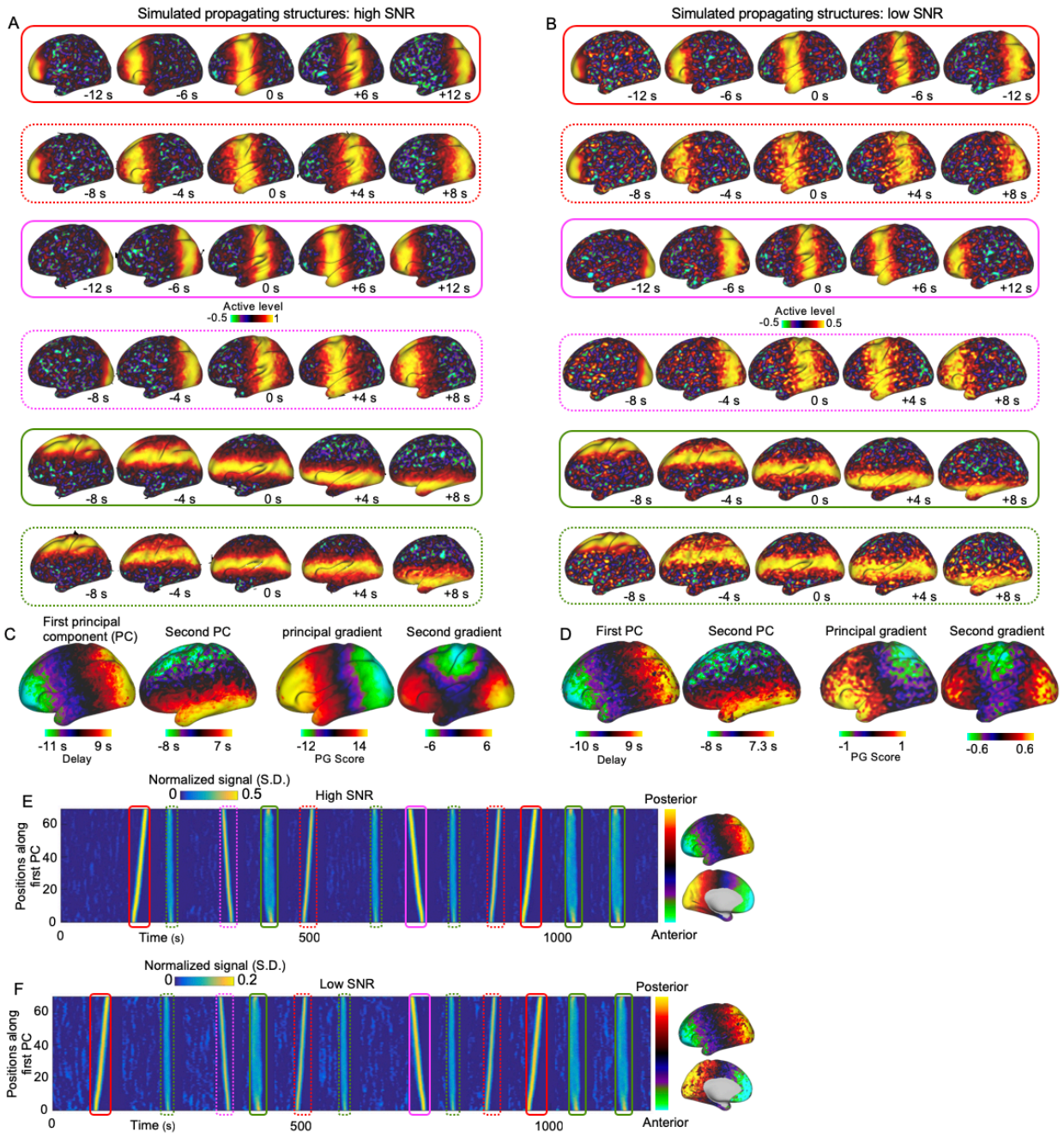

Fig. S3.
The method of decomposing delay profiles can better recover propagating directions than the PG method of embedding the rsfMRI connectivity matrix into a low-dimensional space. We simulated two types of propagating structures along the anterior-posterior direction (red box rows, solid and dashed boxes represent various propagating speed), posterior-anterior direction (magenta box rows), and dorsal-ventral direction (green box rows), one having a high signal-to-noise ratio (SNR) (A), i.e., the level of the active band to the level of background noise, and the other one having low SNR (B). The time zero is when the active band was located at the center of brain surface. Then the simulated propagating structures were randomly inserted into simulated rsfMRI signal

modeled as white noise, generating time series with propagating structures. Applying the method of decomposing delay profiles to both high SNR (2SD, A) and low SNR (5SD, B) simulated time series successfully recovered two propagating directions in (C, left) and (D, left) respectively, indicated by the first two principal components. In contrast, the PG method only recovered one direction in the high SNR simulated data (C, right) and failed to recover any directions in the low SNR simulated data (D, right). Projecting an exemplary time series along the principal delay profile (the first principal component) generated the time-position graphs and showed clear tilted bands in both high SNR (E) and low SNR simulated data (F), indicating the existence of propagating structures along the anterior-to-posterior axis. The different boxes in (E-F) corresponded to different propagations shown in A-B.

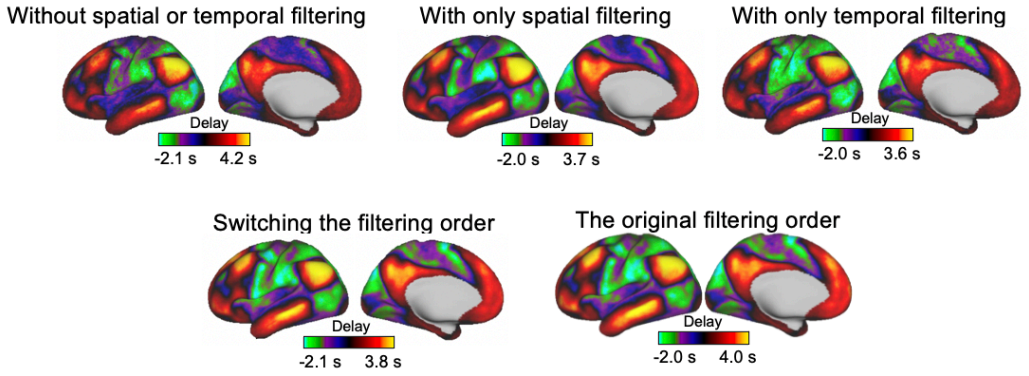

Fig. S4.
The effects of spatial and temporal filtering on the human fMRI using only RL1 session. The principal delay profiles were computed without spatial or temporal filtering, with either spatial or temporal filtering, and with switching the order of filtering, i.e., first applying the temporal filtering and then the spatial filtering, which is opposite to that in Fig. 2 (the original filtering order). The spatial correlation of the principal delay calculated from different filtering schemes with the one calculated using the original filtering order is 0.970, 0.977, 0.974, and 0.997 respectively with all p-value of 0. The spatial correlation of the principal delay profiles in this figure with the one shown in Fig. 2C is 0.951, 0.934, 0.980, 0.979, and 0.984 respectively with all p-value of 0.

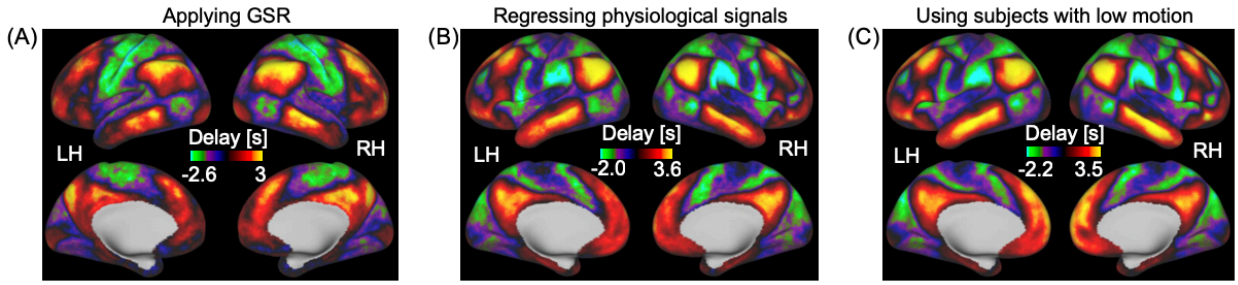

Fig. S5.
Investigating effects of global signal, physiological signals, and motion on the principal delay profile. (A) The principal delay profile calculated using rsfMRI data with applying the global signal regression (GSR) from randomly chosen 100 subjects. (B) The principal delay profile calculated from randomly selected 100 subjects using rsfMRI signal with physiological signals regressed. (C) The principal delay profile calculated from 50 subjects with the lowest head motion. LH, left hemisphere; RH, right hemisphere.

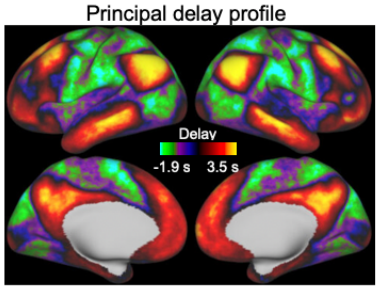

Fig. S6.
The principal delay profile was calculated from randomly chosen 100 subjects using local trough to calculate the delay profile instead of local peak in Fig. 2A. Specifically, we cut rsfMRI signal into time segments based on the peaks of the global mean signal and calculated the delay profile as the relative time delay of the local trough at vertices with respect to the global trough within time segments. Similar cross-hierarchy contrast was observed in the principal delay profile, which might be associated with the negative peak often following the positive peak of the propagation as shown in Fig. 1B.

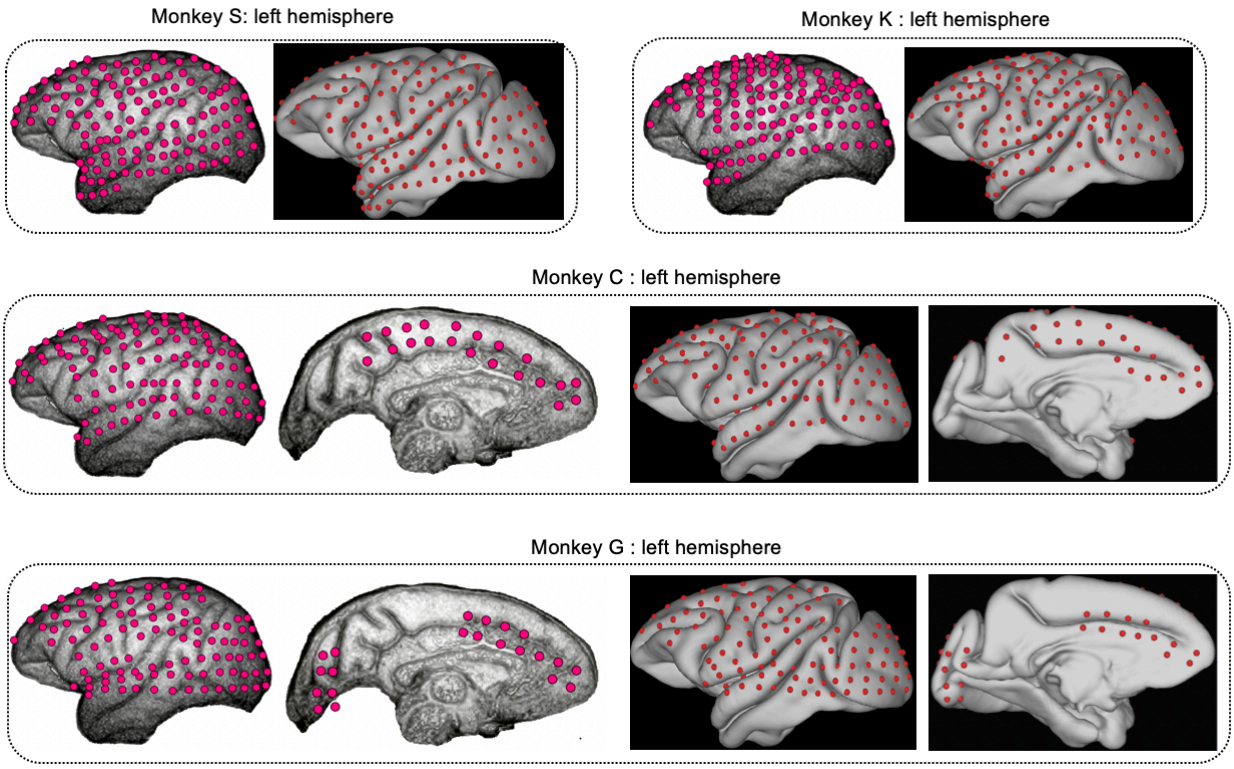

Fig. S7.
The raw 128 electrodes (magenta) of four monkeys were manually mapped onto the average Yerkes19 macaque surface (red electrodes) based on the gyrus and sulci of the brain.

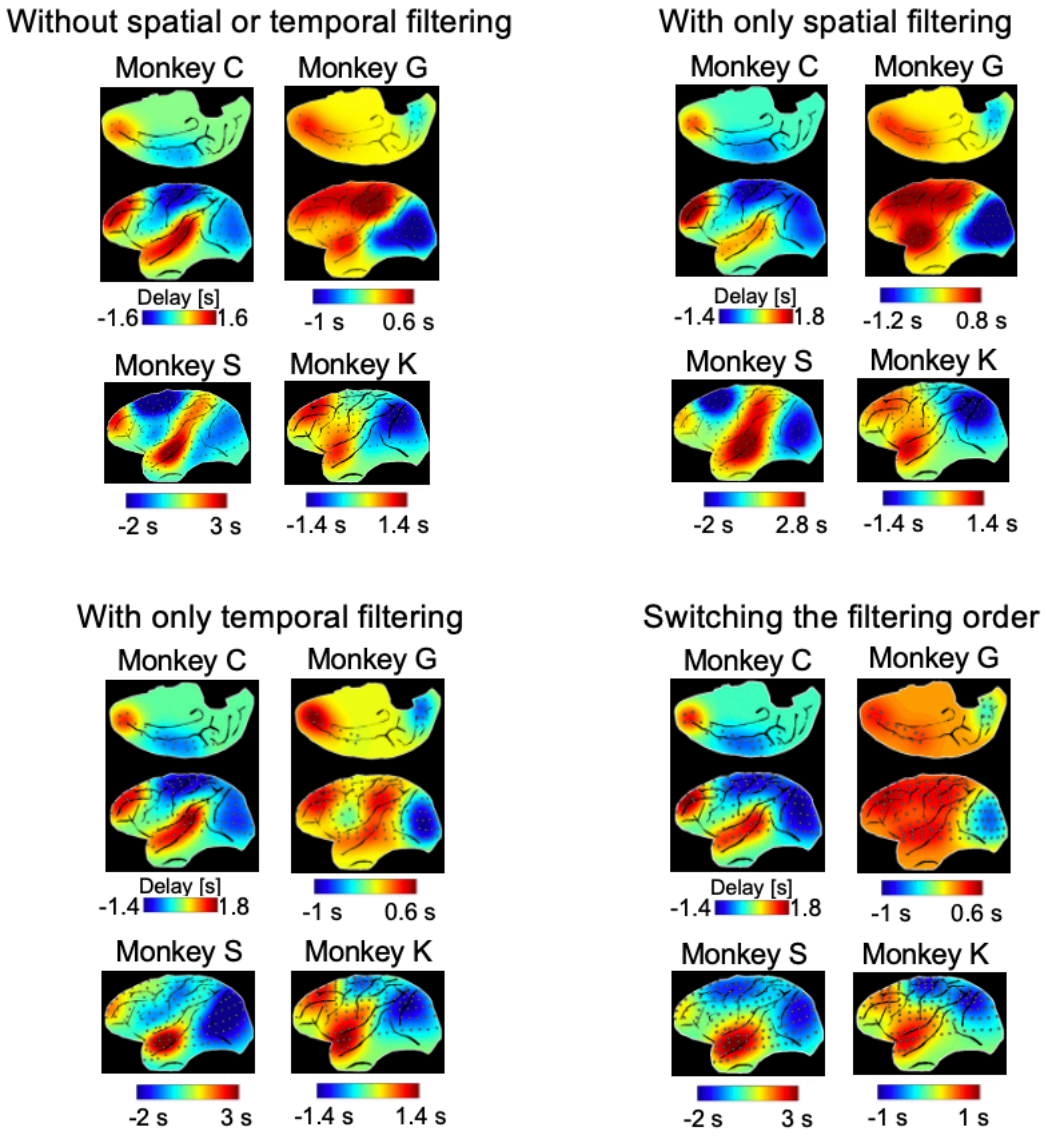

Fig. S8.
The effects of spatial and temporal filtering on the monkey ECoG results. The principal delay profiles were computed without spatial or temporal filtering, with either spatial or temporal filtering, and with switching the order of filtering, i.e., first applying the temporal filtering and then the spatial filtering, which is opposite to that in Fig. 3.

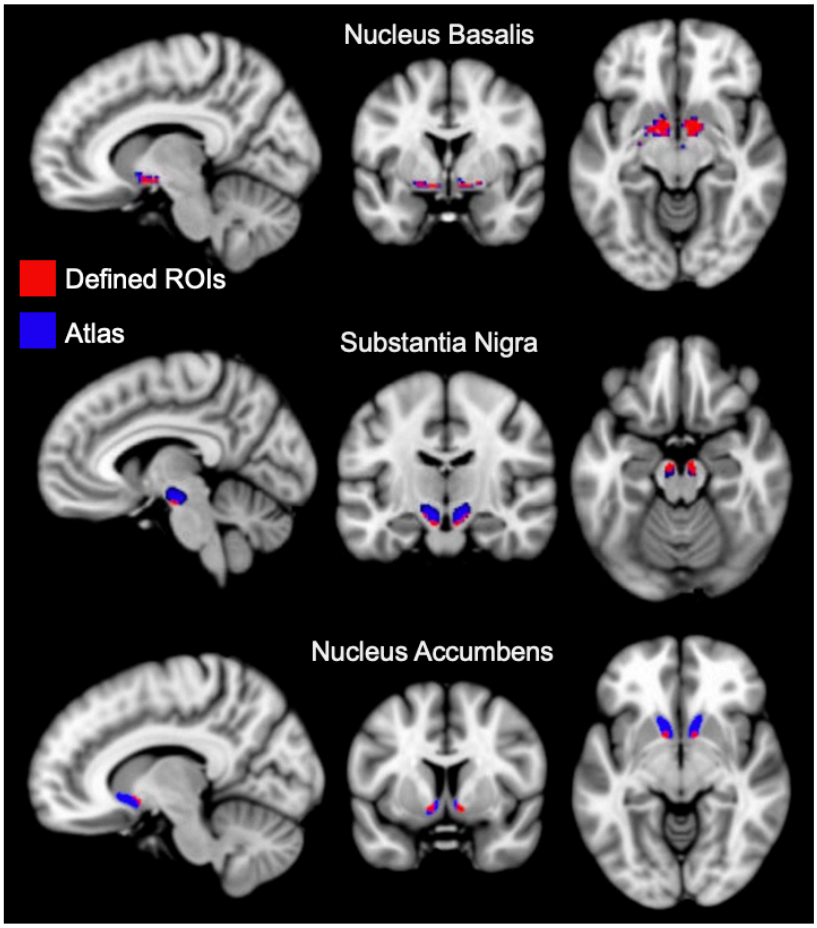

Fig. S9.
The three subcortical ROIs defined in our analysis (red) and the corresponding structures defined by atlases (blue).

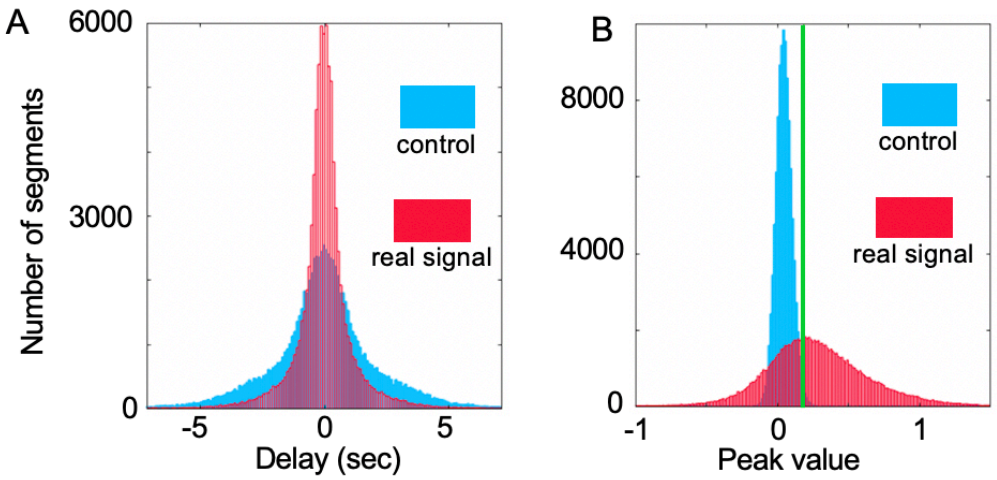

Fig. S10.

Detecting rsfMRI segments with a global involvement. The active band observed in Fig. 1B indicated that the local peaks of different time points within a time segment are clustered together and the phase of local peaks are synchronized. To disrupt the synchronization, we randomly shifted the time series of rsfMRI signal and the global peak value within time segments were recalculated to build a null model as the control group shown in blue. As expected, the delay between the local peak and the global mean peak within segments in real signal are smaller compared to the null distribution (A) and the global peak values are larger in real signal compared to the near-zero values in control group (B). The distribution of delay and peak value from real signal and control group are significantly different (A: $p = 0$, two-sample Kolmogorov-Smirnov test; B: $p = 0$, two-sample Kolmogorov-Smirnov test). The segments with a global involvement (58.80%) are detected if their global signal peak values exceed 99th percentile of null distribution (green vertical line in B).

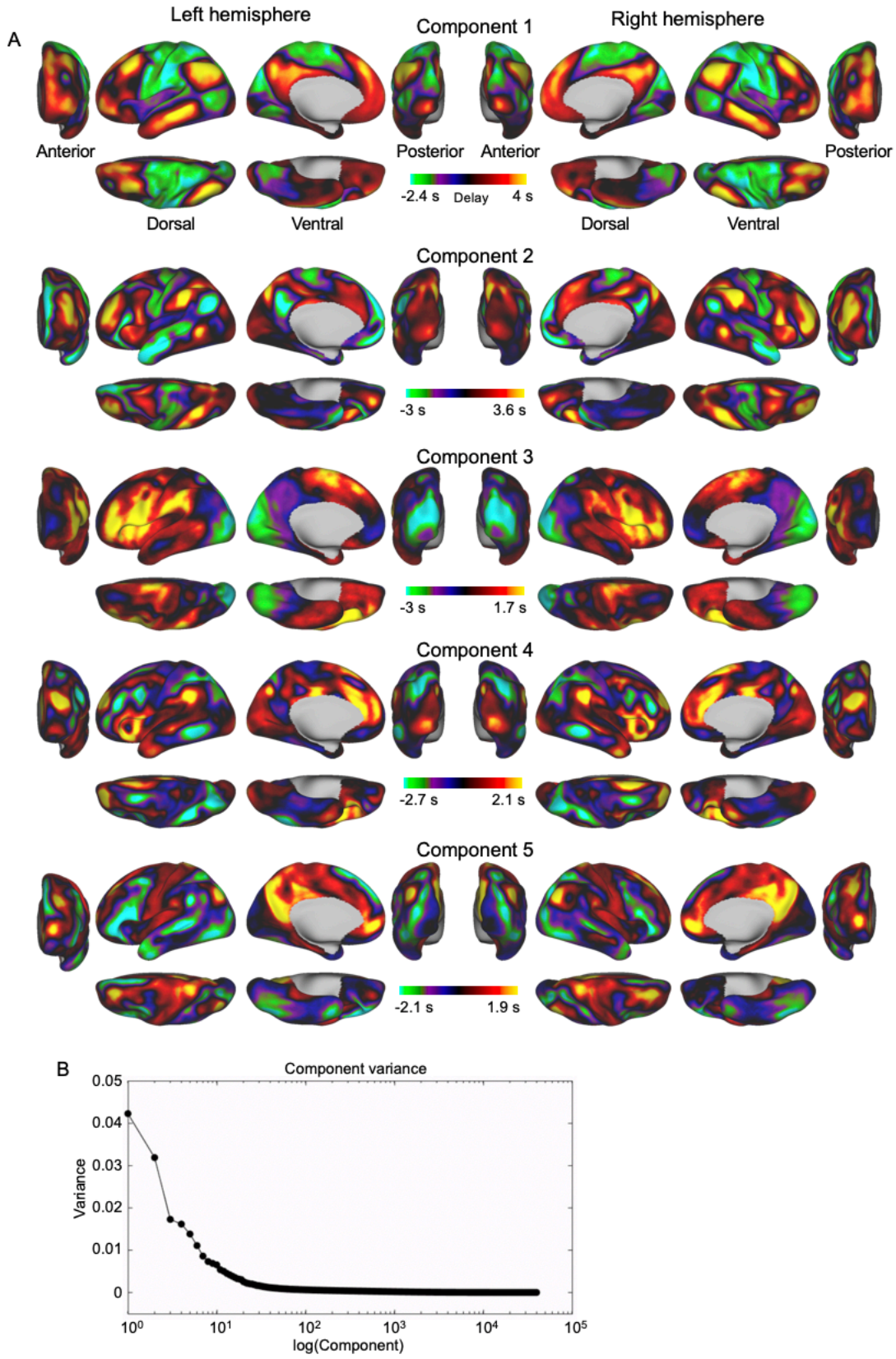
A
Left hemisphere
Component 1
Right hemisphere
Anterior
Posterior
Anterior
Posterior
-2.4 s
Delay
4 s
Dorsal
Ventral
Dorsal
Ventral
Component 2
-3 s
3.6 s
Component 3
-3 s
1.7 s
Component 4
-2.7 s
2.1 s
Component 5
-2.1 s
1.9 s
B
Component variance
Variance
0.05
0.04
0.03
0.02
0.01
0
10^0
10^1
10^2
10^3
10^4
10^5
log(Component)

Fig. S11.
The first 5 principal components (A) explaining the largest variance (B) extracted by applying the method of decomposing delay profiles on all of the four rsfMRI sessions of 460 human subjects.

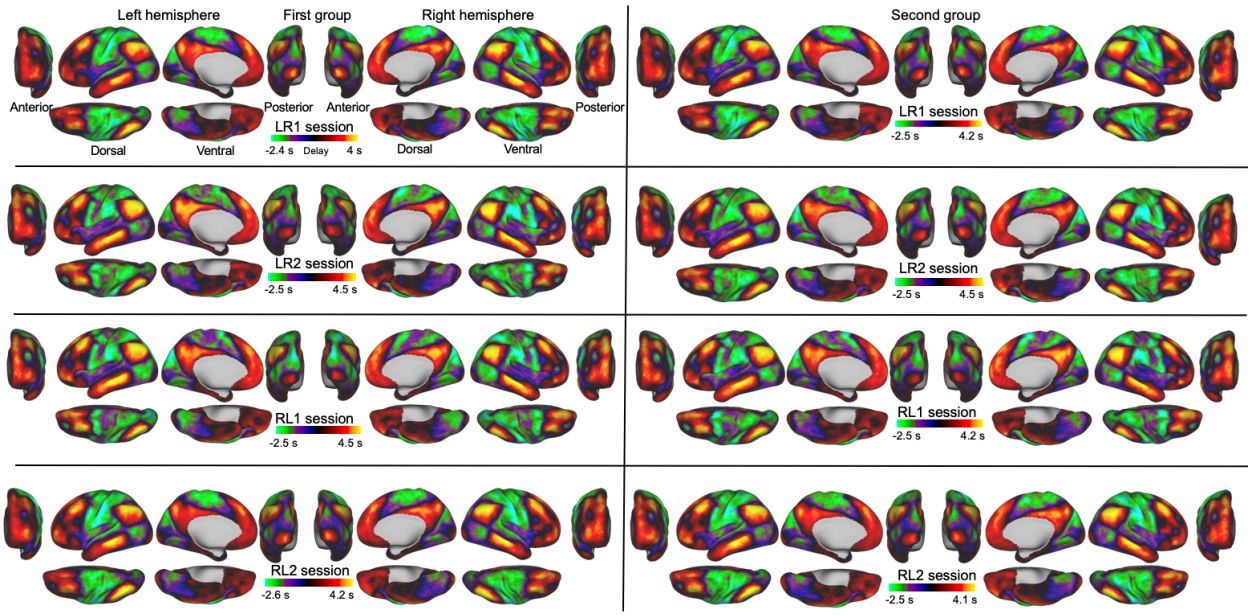

Fig. S12.
The reproducibility of the principal propagating direction along the cross-hierarchy in human rsfMRI. The split-half analyses were applied on each of the four scanning sessions (LR1, LR2, RL1, RL2). Specifically, we randomly split subjects in each scanning session into two equal groups and then applied the method of decomposing delay profiles on each group to extract the first principal component, i.e., the principal delay profile representing the principal propagating direction. All of the computed principal delay profiles showed a cross-hierarchy contrast, similar to the principal delay profile computed from all the four sessions in Fig. 2C. Left: the principal delay profile of the first group from four sessions. Right: the principal delay profile of the second group from four sessions. Each row represents the principal delay profile of the two groups in each session.

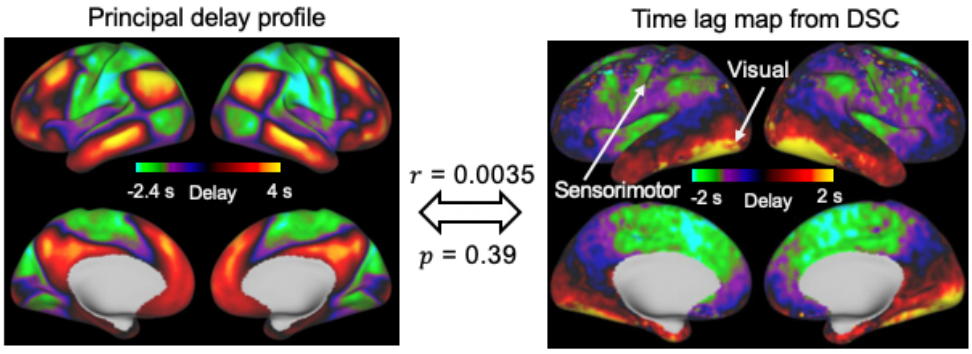

Fig. S13.
A comparison between the principal delay profile of human rsfMRI and the vascular lag map. Left: the principal delay profile from human rsfMRI. Right: the averaged time lag map derived from the dynamic susceptibility contrast (DSC) MRI scan (Tong et al. 2017). The spatial correlation between the two maps is 0.0035 (p = 0.39).

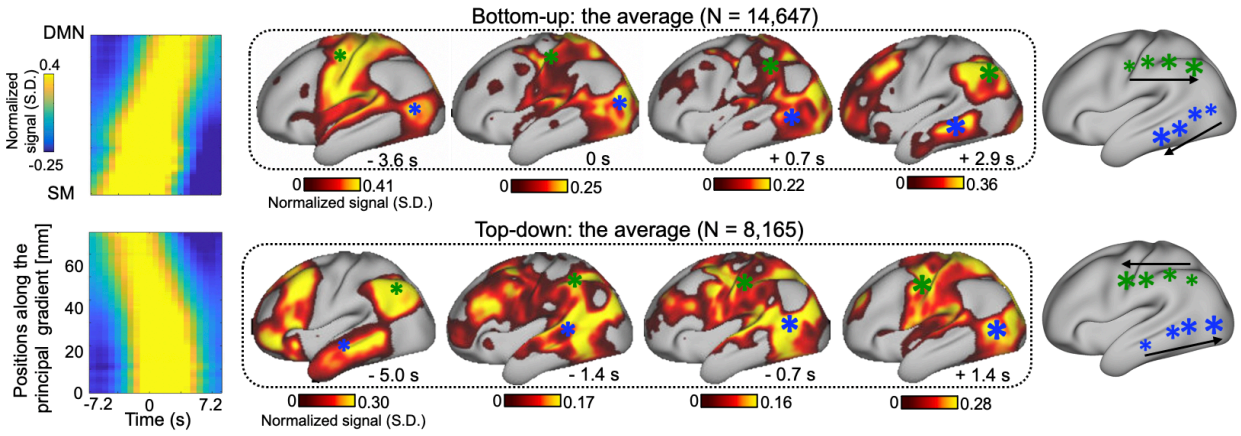

Fig. S14.
The averaged bottom-up (top, N = 14647) and top-down (bottom, N = 8165) propagations detected with respect to the principal gradient are presented on the time-position graphs (left) and the brain surfaces (right).

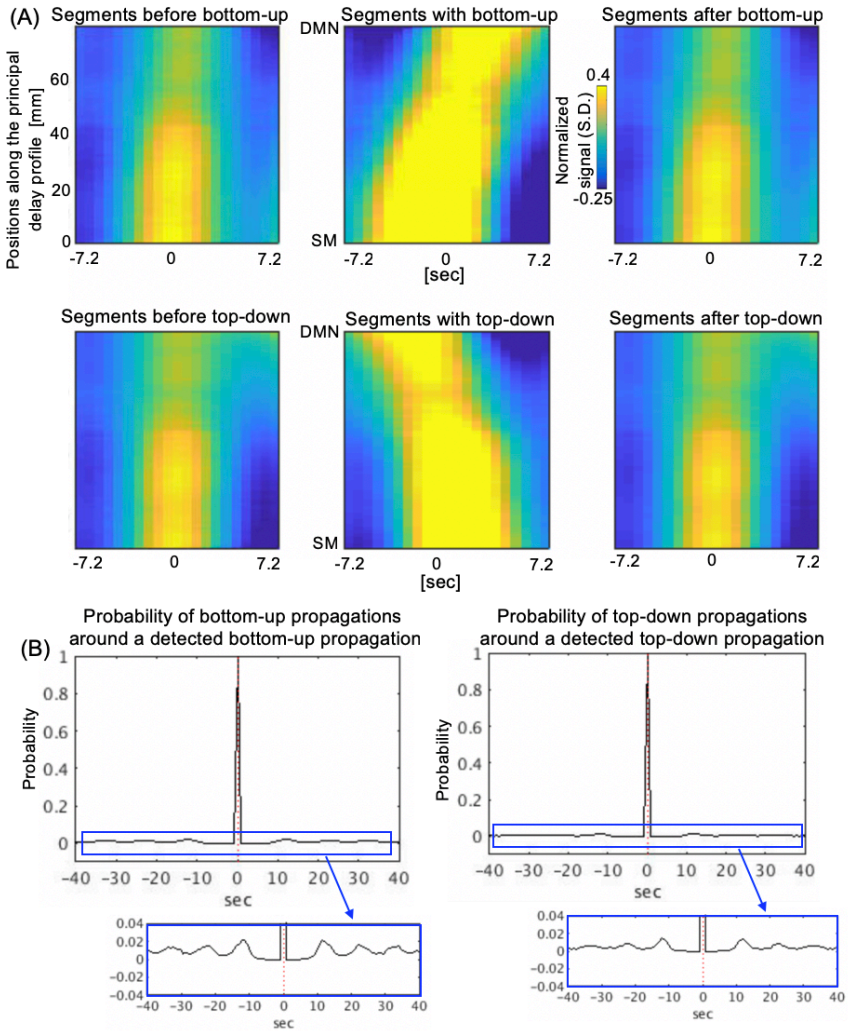

Fig. S15.
The propagations occurred mostly as single and isolated events. (A) The time segments right next to the bottom-up propagations (top) and the top-down propagations (bottom). (B) Left: the occurrence probability of bottom-up propagations around a detected bottom-up propagation. Right: the occurrence probability of top-down propagations around a detected top-down propagation. Small sidelobe peaks around $\pm$12 sec were found particularly in the bottom-up propagations but with small amplitude. Therefore, the propagations mostly occur as isolated events but show some periodicity of ~12 sec when appearing as clusters. A binary time course for each session was produced by assigning 1 to the time points of global positive peaks within time segments with the bottom-up propagations and assigning 0 to other time points. We then calculated the temporal changes of the binary time course, centered at the time points of 1 within an 80-sec time window. The probability of bottom-up propagations around a detected bottom-up propagation was derived by averaging these time windows. Similar analysis was repeated to derive the probability of top-down propagations around a detected top-down propagation.

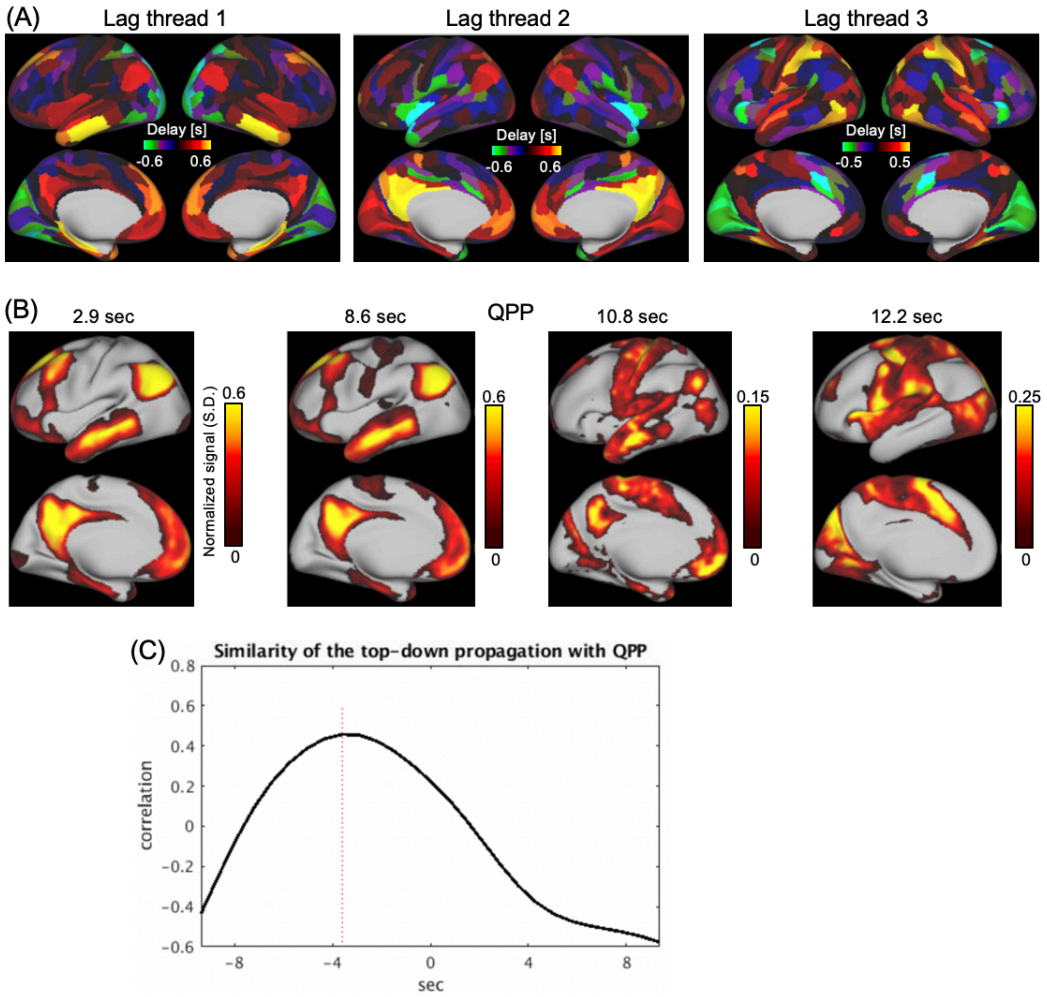

Fig. S16.

We compared our method with the lag thread method and the quasi-periodic patterns (QPP) method. (A) The three lag threads computed from randomly selected 100 subjects using the method from (Mitra et al. 2015). To reduce the dimensionality of the cortical vertices, we used a brain cortical mask (Glasser et al. 2016) to extract the time course of 180 ROIs before calculating the lag thread. The lag thread 1 showed the largest similarity with the principal delay profile ($r = 0.54$ and $p = 10^{-14}$). (B) The QPP computed from randomly chosen 100 subjects based on the method from (Majeed et al. 2011). We randomly chose a consecutive segment with 25 time points as a template. Only the activation regions of the QPP (larger than 0) is shown on the surface. (C) The cross correlation of the averaged top-down propagation in Fig. 2E with the QPP in (B). The highest correlation ($r = 0.46$ and $p = 0$) was found by shifting the top-down propagation by 3.6 sec. When comparing the QPP with the averaged top-down propagation, we extracted the first 21 time points of the QPP so these two have the same 21 time points.

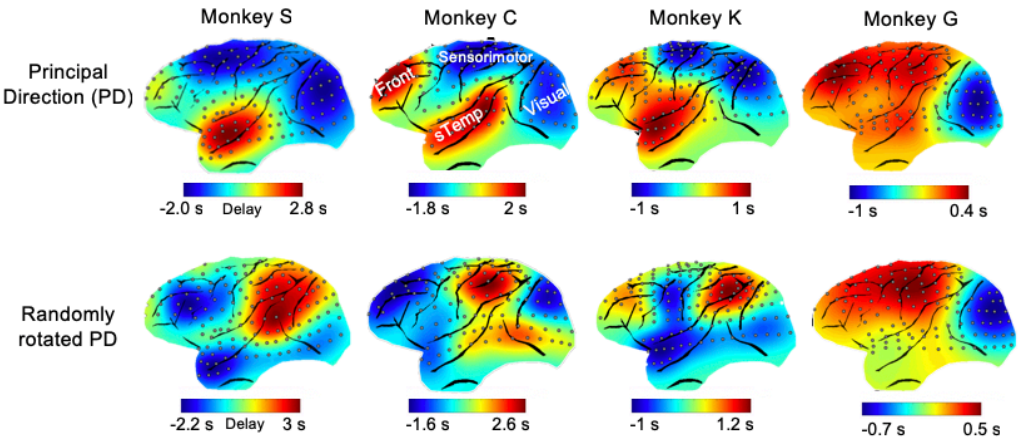

Fig. S17.
The reproducibility of the principal propagating direction along the cross-hierarchy in ECoG gamma-band power. Top panel: the principal delay profile of the ECoG gamma-band (42–95 Hz) power from four monkeys. Bottom panel: the corresponding randomly rotated principal delay profile from four monkeys. Note that all of the principal delay profiles are the first principal component generated by applying the method of decomposing delay profiles except that the one in Monkey S is the second principal component.

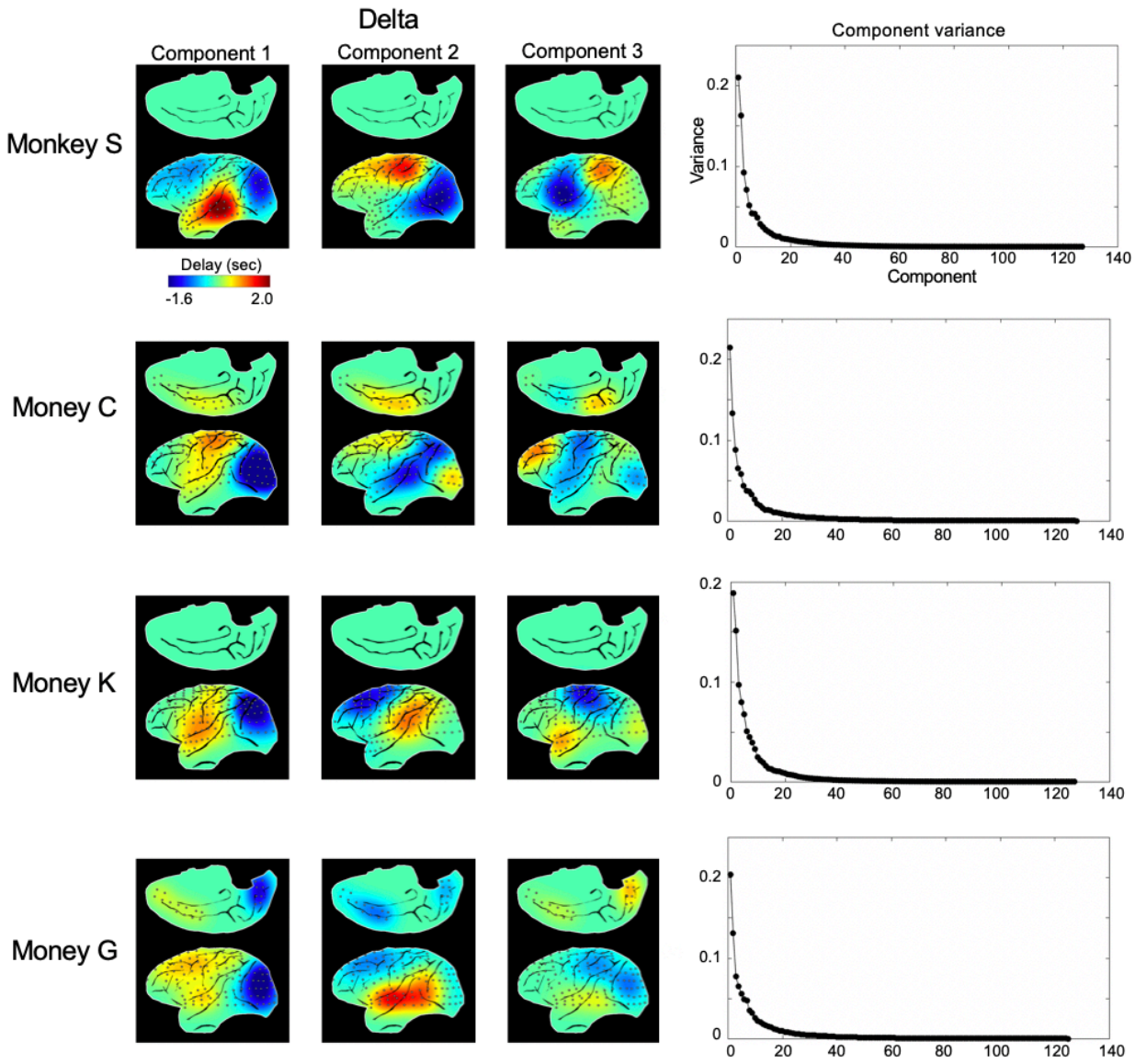

Fig. S18.
The first three principal components explaining the largest variance extracted by applying the method of decomposing delay profiles within the delta frequency band (1–4 Hz) for each monkey. Right: the variance explained by each component.

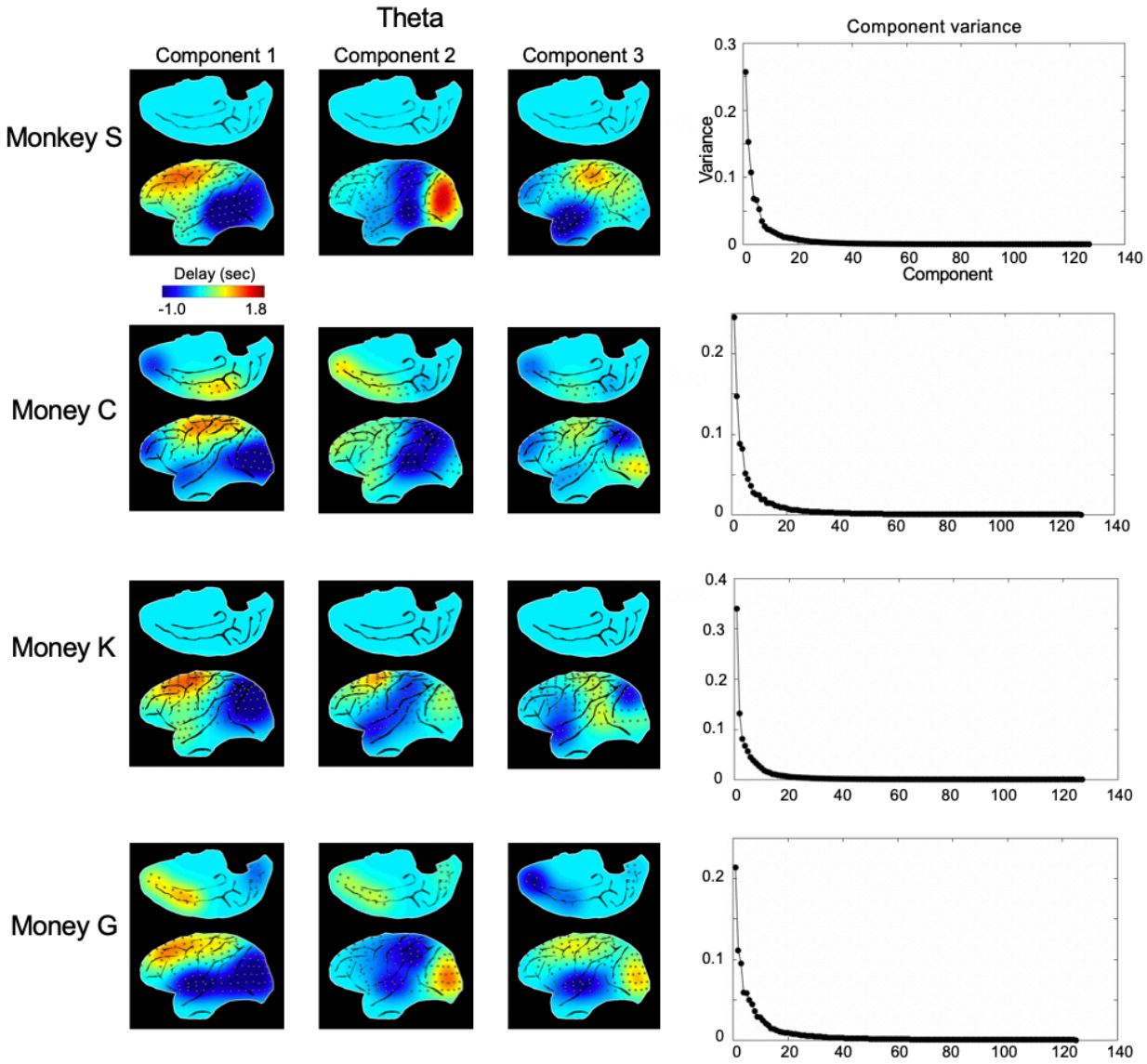

Fig. S19.
The first three principal components explaining the largest variance extracted by applying the method of decomposing delay profiles within the theta frequency band (5–8 Hz) for each monkey. Right: the variance explained by each component.

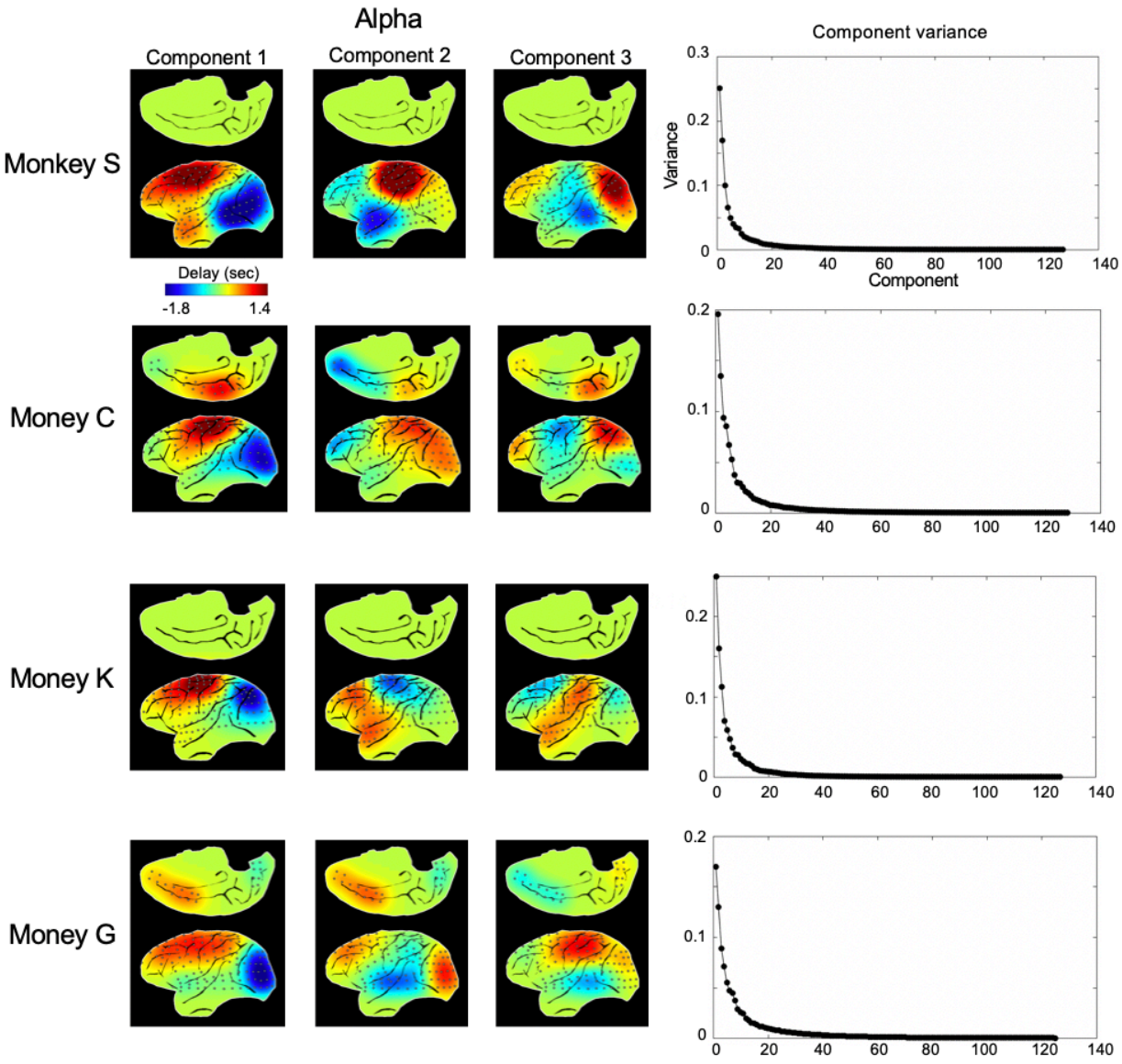

Fig. S20.
The first three principal components explaining the largest variance extracted by applying the method of decomposing delay profiles within the alpha frequency band (9–15 Hz) for each monkey. Right: the variance explained by each component.

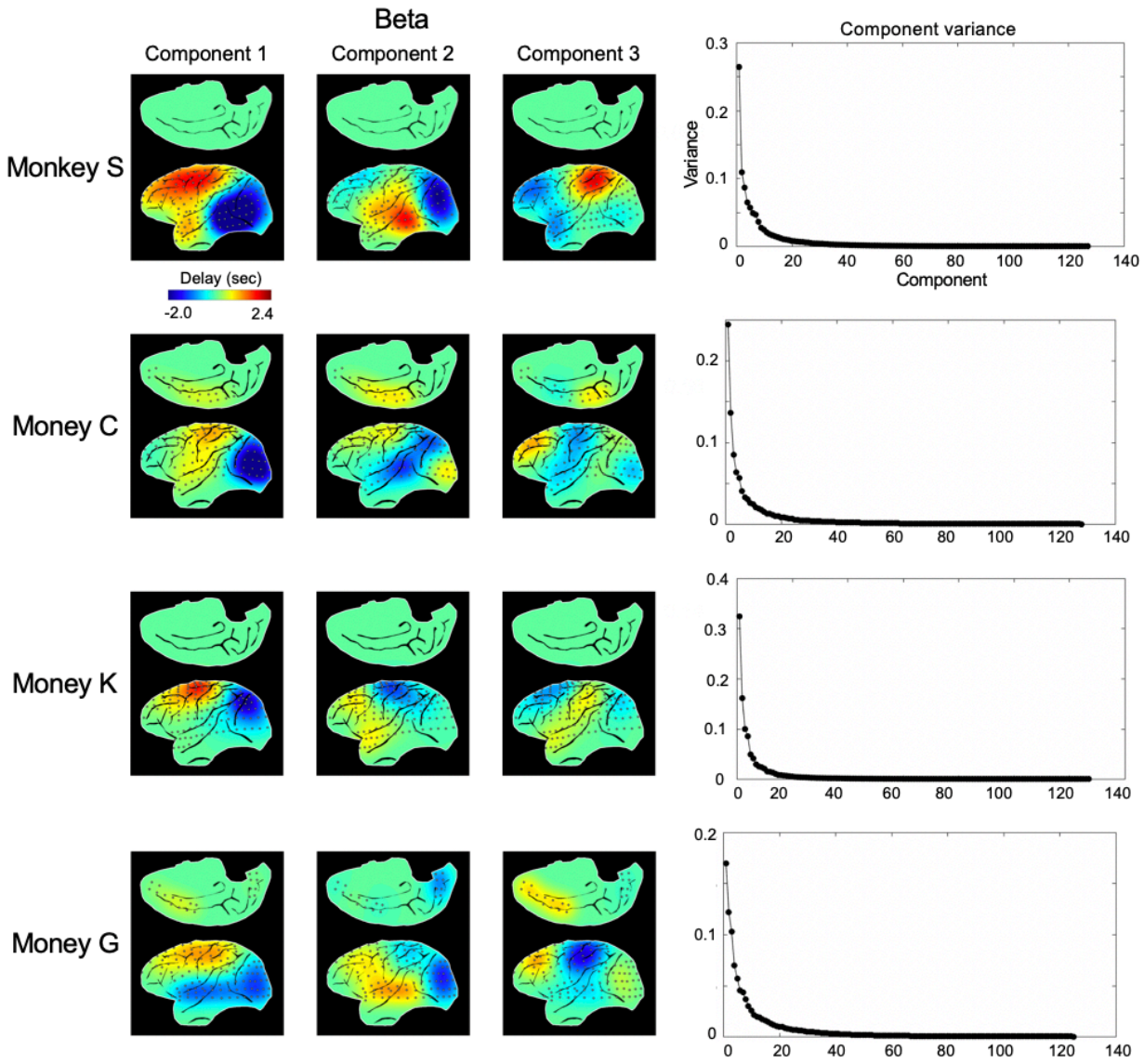

Fig. S21.
The first three principal components explaining the largest variance extracted by applying the method of decomposing delay profiles within the beta frequency band (17–32 Hz) for each monkey. Right: the variance explained by each component.

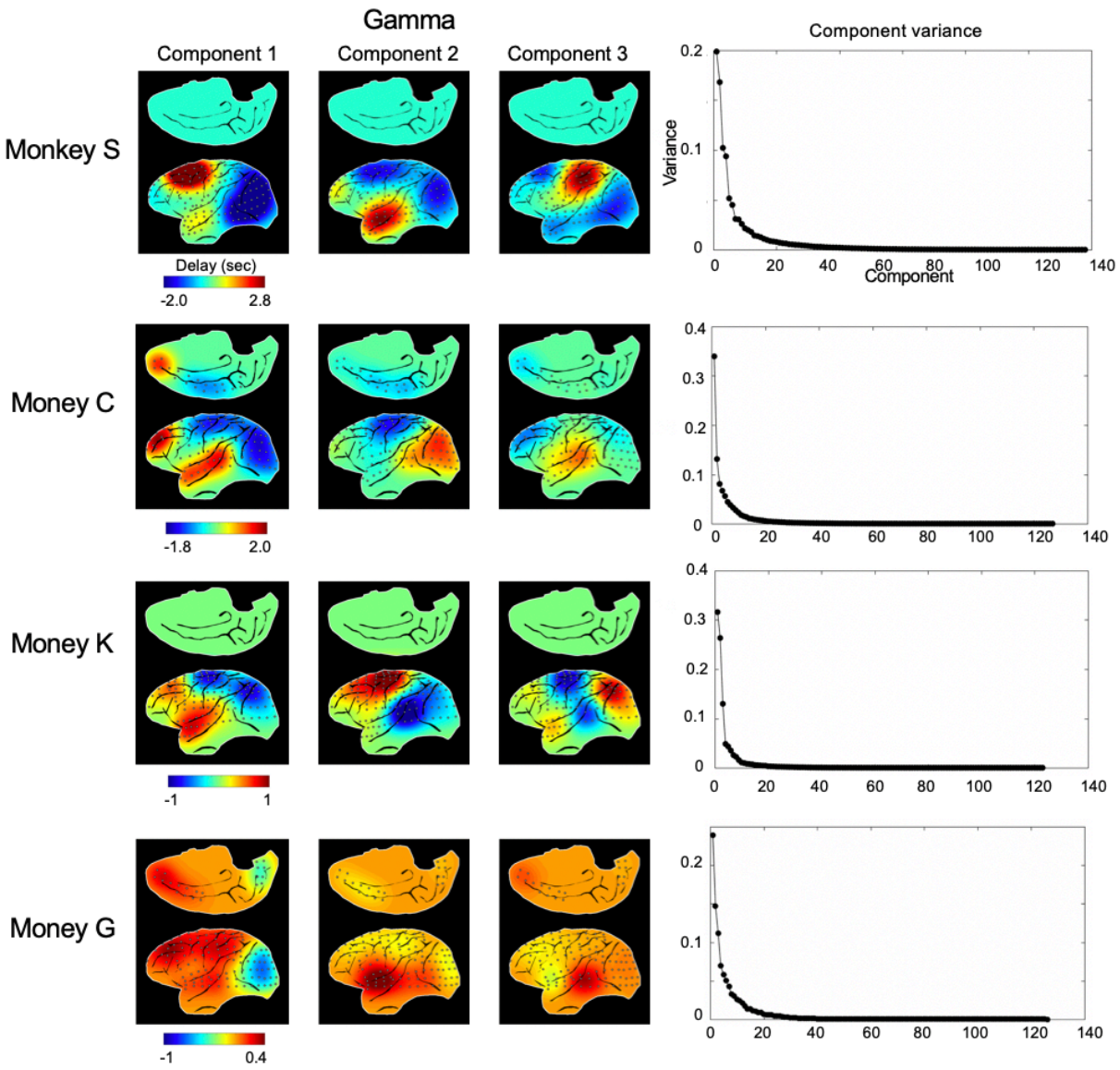

Fig. S22.
The first three principal components explaining the largest variance extracted by applying the method of decomposing delay profiles within the gamma frequency band (42–95 Hz) for each monkey. Right: the variance explained by each component.

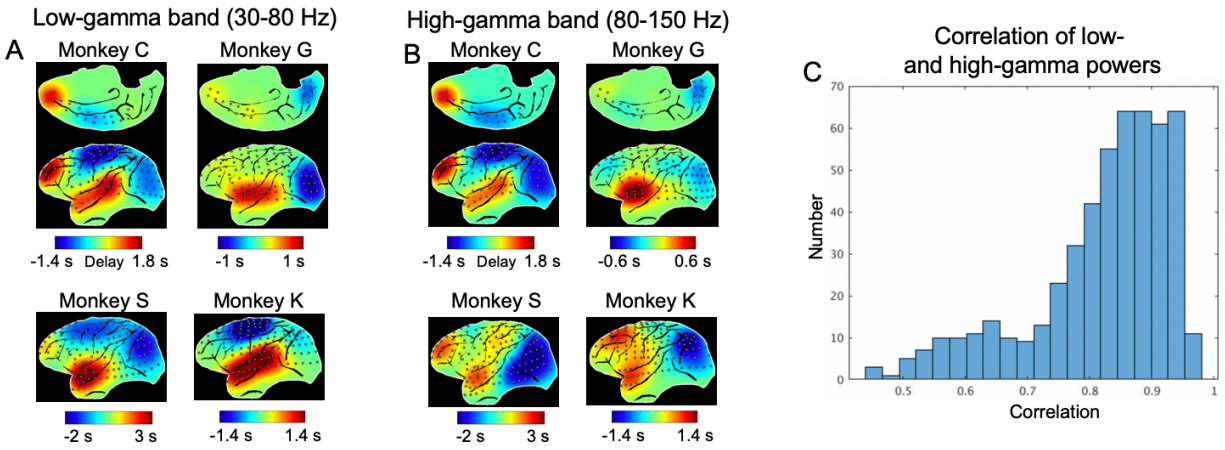

Fig. S23.
The principal delay profiles of two sub-bands of the gamma range. (A) The principal delay profile of the low-gamma band (30-80 Hz) power in monkey ECoG shows a cross-hierarchy contrast. (B) The similar result for the high-gamma band (80-150 Hz) power of monkey ECoG. (C) The temporal correlations between the low-gamma and high-gamma powers for all the electrodes from all 4 monkeys.

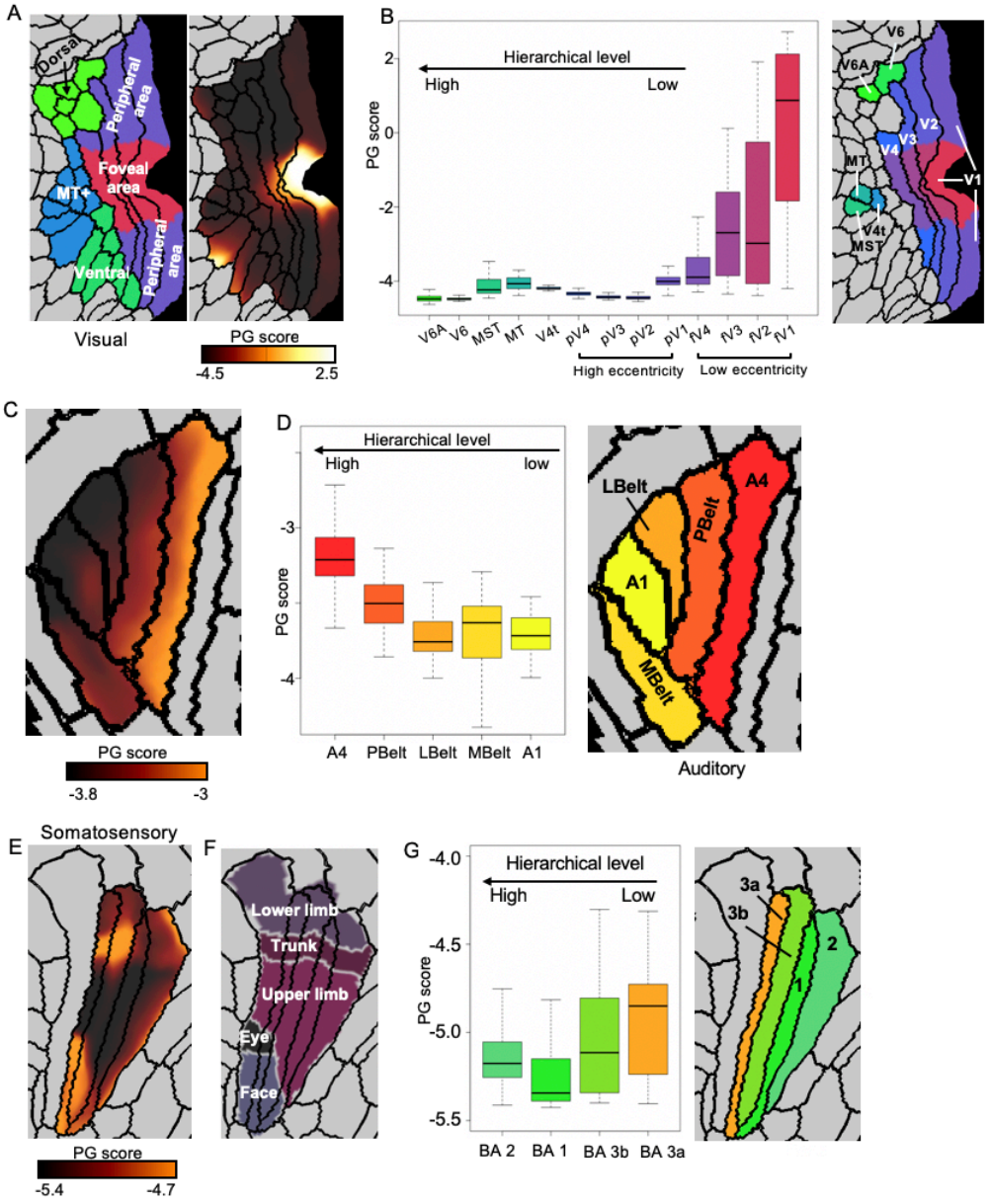

Fig. S24.

The relationship between the principal gradient (PG) score and the hierarchical level within each sensory modality. (A) The local contrast of the principal gradient within the three visual-related regions (MT+ complex, Dorsal stream, Ventral stream) defined by a multi-modal parcellation atlas (Glasser et al. 2016). (B) The averaged PG score of 13 visual parcels that were arranged according to their hierarchical (Felleman 2009) and retinotopic relationships (Benson et al. 2018). The simple linear regression indicated a significant relationship between the PG score and the hierarchy level across brain regions ($p = 5.5\text{x}10^{-113}$ for fV1-fV2-fV3-fV4-V4t-MT-MST-V6-V6A and $p = 2.5\text{x}10^{-253}$ for pV1-pV2-pV3-pV4-V4t-MT-MST-V6-V6A). (C-D) Results for the auditory system indicated a similar contrast between the primary and association auditory areas. The simple linear regression indicated a significant relationship between the PG score and the hierarchy level across auditory regions ($p = 2.8\text{x}10^{-206}$). (E-G) Results for the somatosensory system. (E-F) The contrast of the principal gradient also shows certain correspondence with the somatotopic arrangement

(Van Essen and Glasser 2018). (G) The simple linear regression indicated a significant relationship between the PG score and the hierarchy level across somatosensory regions (p = $8.8x10^{-66}$). Abbreviation: Dorsal, dorsal stream. Ventral, ventral stream. V6A, area V6A. V6, sixth visual area. MT+, MT+ complex. MST, medial superior temporal area. MT/V5, middle temporal area/fifth visual area. V4t, V4 transition zone. pV4, peripheral fourth visual area. pV3, peripheral third visual area. pV2, peripheral second visual area. pV1, peripheral primary visual cortex. fV4, foveal fourth visual area. fV3, foveal third visual area. fV2, foveal second visual area. fV1, foveal primary visual cortex. V4, fourth visual area. V3, third visual area. V2, second visual area. V1, primary visual cortex. A4, auditory 4 complex. PBelt, parabelt complex. LBelt, lateral belt complex. MBelt, medial belt complex. A1, primary auditory cortex. BA2, Brodmann's area 2. BA1, Brodmann's area 1. BA 3b, Brodmann's area 3b. BA 3a, Brodmann's area 3b. FEF, frontal eye fields. IPS, intraparietal sulcus area.

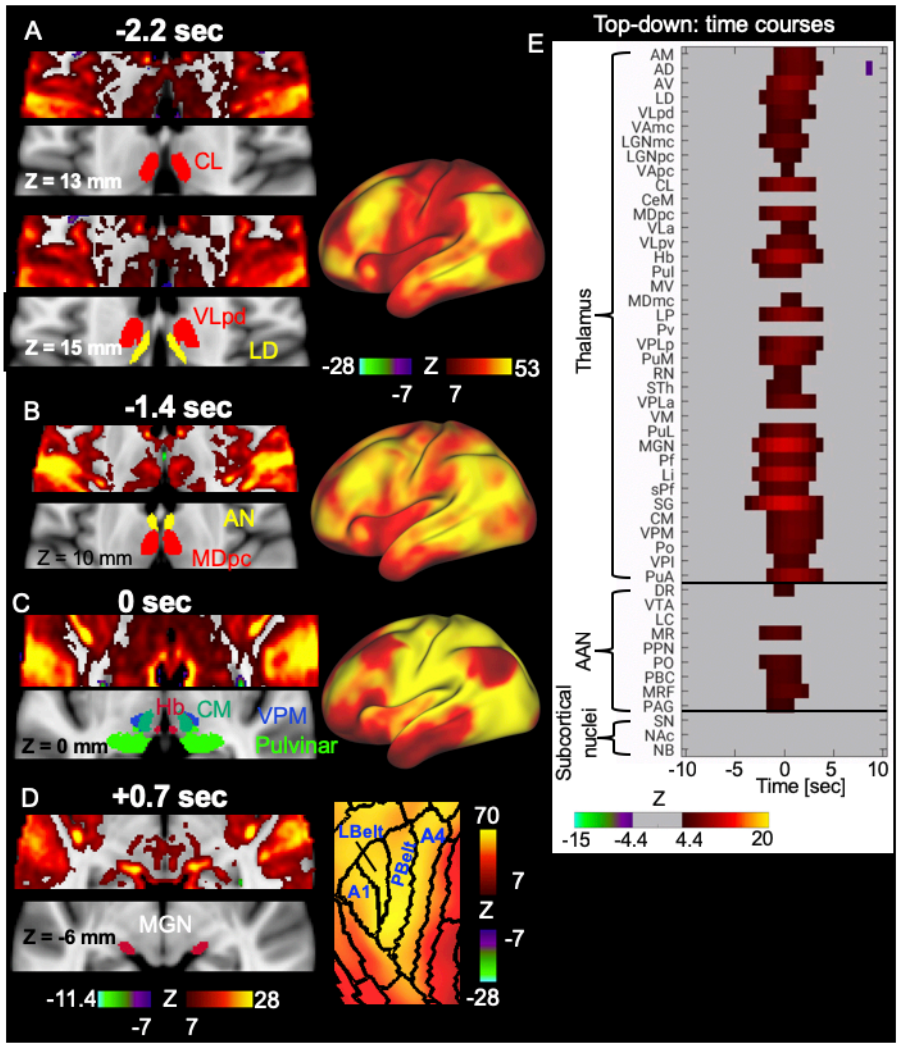

Fig. S25.
The relationship between subcortical co-activations and the top-down propagation. The location of the thalamic nuclei was based on the Morel Atlas (Krauth et al. 2010). The time is with respect to the global mean peak. (A-D) The thalamic co-activations at different phases of the top-down propagations show a correspondence with the cortical changes. (A) The co-activation of the DMN is associated with the thalamic co-activations in the CL, VLpd and LD. (B) The co-activation of the DMN is associated with the thalamic co-activations in the AN and MDpc. (C) The co-activation of the sensory/motor is associated with the thalamic co-activations in the Hb, CM, VPM, and pulvinar. (D) The co-activations of MGN is associated with the auditory co-activation (A1, Lbelt, Pbelt, A4). (E) The temporal dynamics of all the subcortical regions. The

Z-score time courses were averaged within 37 thalamic regions of interest (ROIs) defined by the Morel's atlas and 9 brainstem ROIs defined by the ANN atlas, as well as the three ROIs (SN, NAc, NB) we defined by combining our results with brain atlas (Desikan et al. 2006; Keuken and Forstmann 2015; Liu et al. 2018). The time courses within each group of ROIs were sorted according to their values at t = -5.8 sec. The q-value generated by FDR corresponding to z-score 4.4 and 7 is 10^{-5} and $7.4x10^{-13}$ respectively. Abbreviation: MDmc, mediodorsal nucleus magnocellular part. MDpc, mediodorsal nucleus parvocellular part. MV, medioventral nucleus. CL, central lateral nucleus. CeM, central median nucleus. CM, centre median nucleus. Pv, paraventricular nucleus. Hb, Habenular nucleus. Pf, parafascicular nucleus. sPf, subparafascicular nucleus. PuM, medial pulvinar. PuI, inferior pulvinar. PuL, lateral pulvinar. PuA, anterior pulvinar. LP, lateral posterior nucleus. MGN, medial geniculate nucleus. SG, supragenicular nucleus. Li, limitans nucleus. Po, posterior nucleus. LGN, lateral geniculate nucleus. VPLa, ventral posterior lateral nucleus anterior part. VPLp, ventral posterior lateral nucleus posterior part. VPM, ventral posterior medial nucleus. VPI, ventral posterior inferior nucleus. VLa, ventral lateral anterior nucleus. VLpd, ventral lateral posterior nucleus dorsal part. VLpv, ventral lateral posterior nucleus ventral part. VAmc, ventral anterior nucleus magnocellular part. VApc, ventral anterior nucleus parvocellular part. VM, ventral medial nucleus. AD, anterior dorsal nucleus. AM, anterior medial nucleus. AV, anterior ventral nucleus. LD, lateral dorsal nucleus. AN, anterior nucleus. STh, subthalamic nucleus. DR, dorsal raphe. VTA, ventral tegmental area. LC, locus coeruleus. MR, median raphe. PPN, pedunculopontine nucleus. PO, pontis oralis. PBC, parabrachial complex. MRF, midbrain reticular formation. PAG, periaqueductal gray. NAc, nucleus accumbens. NB, nucleus Basalis. SN, substantia Nigra. A4, auditory 4 complex. PBelt, parabelt complex. LBelt, lateral belt complex. A1, primary auditory cortex. SM, sensory/motor. DMN, default mode network.

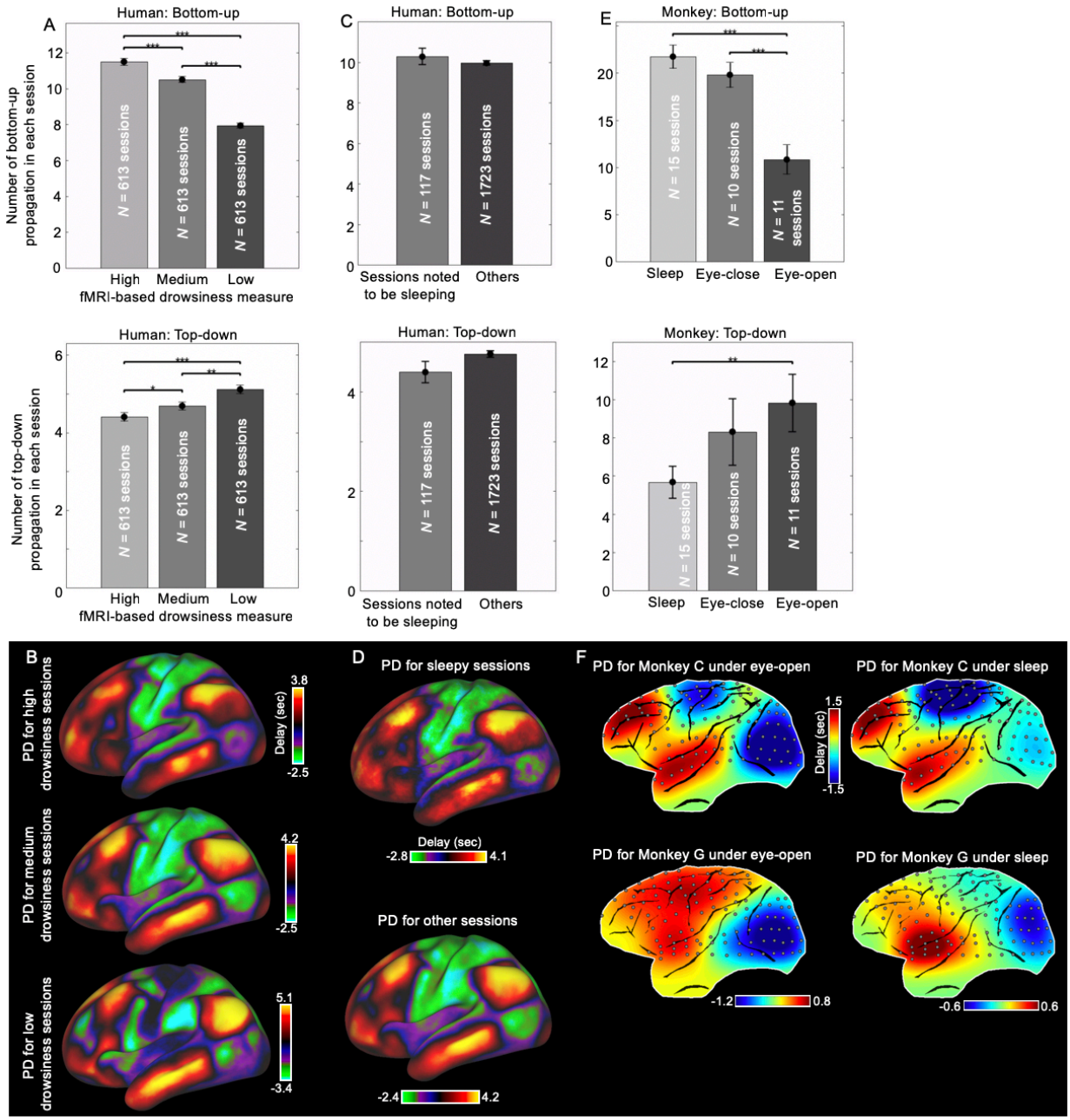

Fig. S26.

The low arousal level is related with less top-down and more bottom-up propagation activity. (A) More top-down propagation (bottom panel) and less bottom-up (top panel) propagation is significantly observed in three groups of human rsfMRI sessions with decreasing drowsiness levels as measured by an fMRI-based drowsiness index (Gu et al. 2020). The three equal groups of sessions with low, medium, high drowsiness levels were formed by sorting all the four rsfMRI sessions from 460 subjects based on their drowsiness level. We then quantified the number of top-down and bottom-up propagations in each session and compared their propagation number in different groups. The error bars represent the standard deviation of the propagation number across

sessions in each group. The number of time segments of global involvement during analysis for each group: low (N = 19578), medium drowsiness group (N = 21409), high drowsiness group (N = 22406). (B) The principal delay profile is extracted for each group in (A) and all of them showed a strong contrast between the sensory/motor areas and the default mode network, similar with that extracted using all sessions in Fig. 2C. (C) The same trend is also observed in a group of rsfMRI sessions (117 sessions) where subjects were noted to be sleeping during scanning compared to other rsfMRI sessions. The number of time segments of global involvement for analysis in sleepy sessions and other sessions is 4137 and 58957 respectively. (D) The principal delay profile is extracted from the group of sessions noted to be sleeping and the other sessions in (C) respectively and both of them showed a strong contrast between the sensory/motor areas and the default mode network, similar with that extracted using all sessions in Fig. 2C. (E) The number of the top-down propagation and the bottom-up propagation in the ECoG gamma powers shows a similar and significant trend across the eyes-open, eyes-closed, and sleep sessions using ECoG gamma-band powers concatenated from all of the four monkeys. The number of time segments of global involvement used in eyes-open, eyes-closed and sleep is 588, 595 and 901 respectively. (F) The principal delay profile is extracted under eyes-open or sleep conditions from the ECoG gamma powers for monkey C and monkey G respectively. The ECoG data under both eyes-open and sleep conditions were recorded only in monkey C and monkey G. All of them showed a strong contrast between the sensory/motor areas and the high-order regions, similar with that extracted under eyes-closed conditions in Fig. 3A. Note that the principal delay profile for the human rsfMRI signals in (C-D) is the first principal component; the principal delay profile for the Monkey C under eyes-open condition and sleep condition is the second and the first principal component respectively; the principal delay profile for the Monkey G under eyes-open condition and sleep condition is the first and the second principal component respectively. Each session is 15 minutes and 25 minutes in length for the human rsfMRI data (A-D) and ECoG gamma band powers (E-F) respectively. Error bars represent the standard error of the mean (SEM). Asterisks represent the level of significance: *: $0.01 < p \leq 0.05$; **: $0.001 < p \leq 0.01$; ***: $p \leq 0.001$.

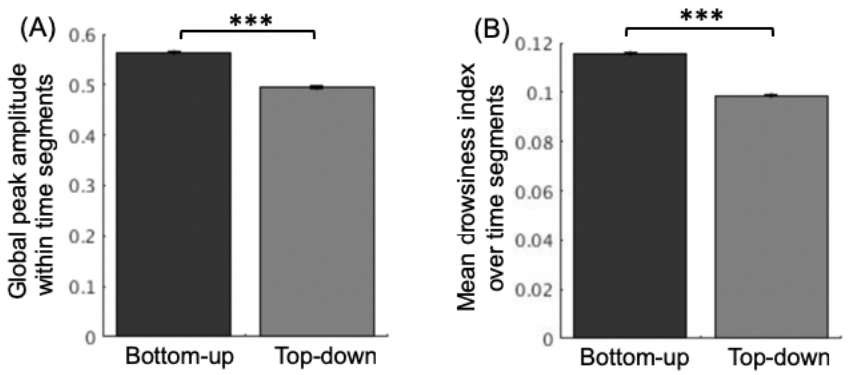

Fig. S27.
We calculated the global positive peak amplitude within time segments with propagations (A) and mean drowsiness index over time segments with propagations (B). The bottom-up propagations showed significantly larger global peak amplitude (p-value = 0) and higher drowsiness index (p-value = 0) than the top-down propagations.

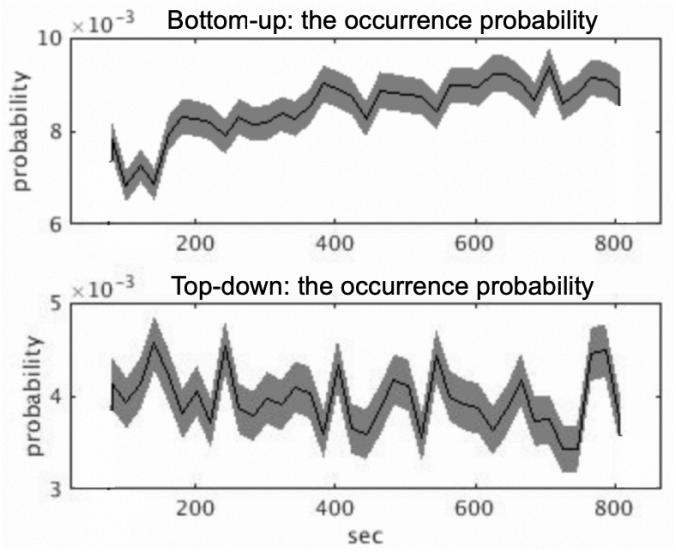

Fig. S28.
The occurrence probability of the bottom-up and top-down propagations over the course of resting-state scanning. A binary time course for each session was produced by assigning 1 to the time points of global positive peaks within time segments with the bottom-up propagations and assigning 0 to other time points. To compute the occurrence probability of the bottom-up

propagations over the course, we averaged the binary time course over all sessions and down sampled every 20 seconds to reduce the noise. Similar analysis was repeated with the top-down propagations to compute their occurrence probability. The occurrence probability of the bottom-up propagations was found to significantly increase over time in a linear regression model (p-value = 0, F-test) whereas the occurrence probability of the top-down propagations not (p-value = 0.18, F-test). The first 76 and the last 79 time points were skipped since they appearing earlier or later than the first or last trough of the global signal were not included during the analysis. The shadow represents regions within one standard error of the mean.

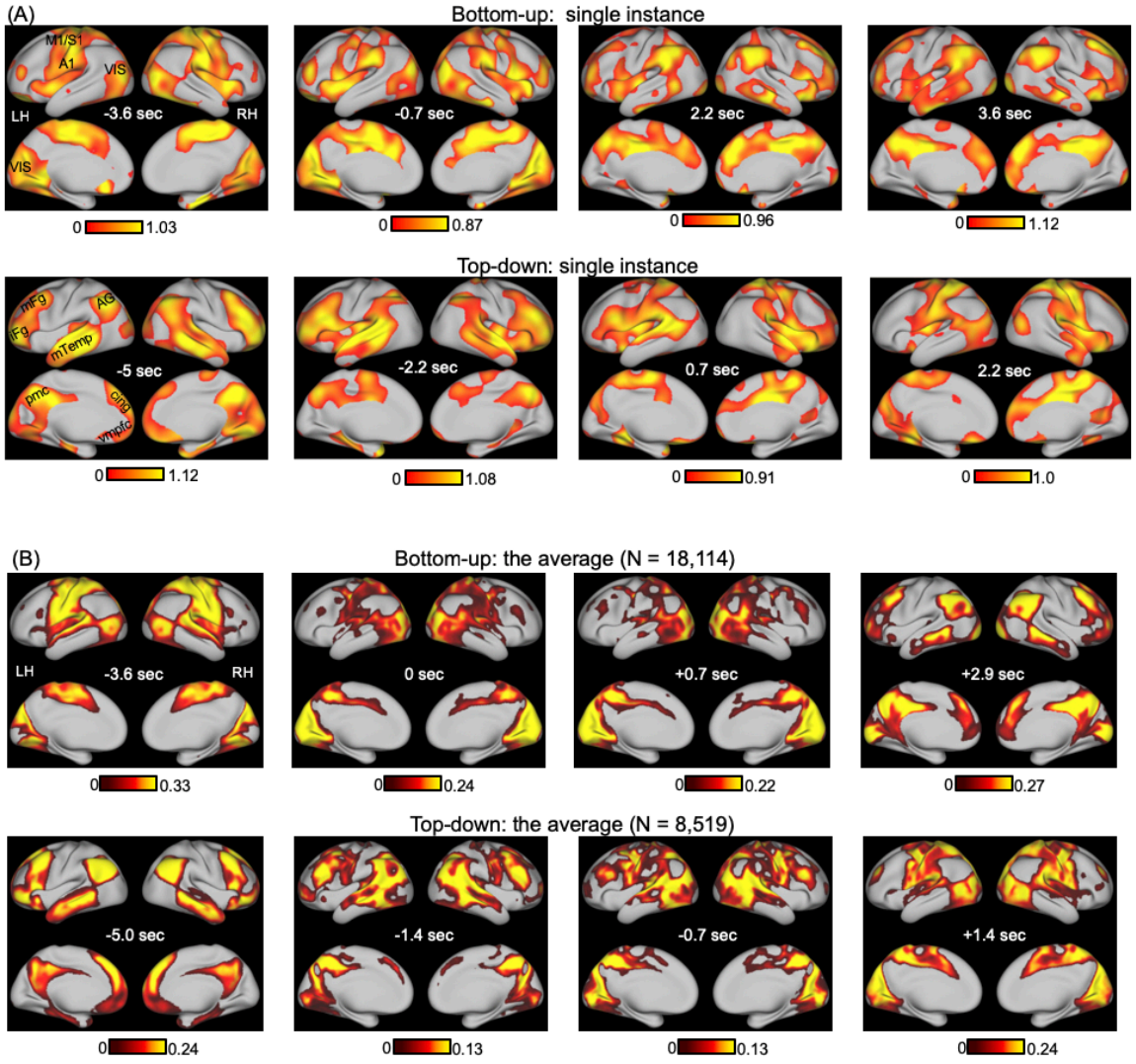

Fig. S29.
(A) The same exemplary rsfMRI segments with propagations in Fig. 1C showing both lateral and medial surfaces in two hemispheres. (B) The same averaged propagations in Fig. 2E showing both lateral and medial surfaces in two hemispheres. Abbreviation: VIS, visual cortex; M1, primary motor cortex; S1, primary somatosensory cortex; A1, primary auditory; iFG, inferior frontal gyrus; mFG, middle frontal gyrus; AG, angular gyrus; mTemp, middle temporal cortex; pmc, posteromedial cortex; cing, anterior cingulate cortex; vmpfc, ventromedial prefrontal cortex; LH, left hemisphere; RH, right hemisphere.

References:

Benson NC, Jamison KW, Arcaro MJ, Vu AT, Glasser MF, Coalson TS, Van Essen DC, Yacoub E, Ugurbil K, Winawer J, Kay K. 2018. The Human Connectome Project 7 Tesla retinotopy dataset: Description and population receptive field analysis. J Vis. 18:1–22.

Desikan RS, Ségonne F, Fischl B, Quinn BT, Dickerson BC, Blacker D, Buckner RL, Dale AM, Maguire RP, Hyman BT, Albert MS, Killiany RJ. 2006. An automated labeling system for subdividing the human cerebral cortex on MRI scans into gyral based regions of interest. Neuroimage. 31:968–980.

Felleman DJ. 2009. Extrastriate Visual Cortex. In: Binder MD,, Hirokawa N,, Windhorst U, editors. Encyclopedia of Neuroscience. Berlin, Heidelberg: Springer Berlin Heidelberg. p. 1526–1532.

Glasser MF, Coalson TS, Robinson EC, Hacker CD, Harwell J, Yacoub E, Ugurbil K, Andersson J, Beckmann CF, Jenkinson M, Smith SM, Van Essen DC. 2016. A multi-modal parcellation of human cerebral cortex. Nature.

Gu Y, Han F, Sainburg LE, Liu X. 2020. Transient Arousal Modulations Contribute to Resting-State Functional Connectivity Changes Associated with Head Motion Parameters. Cereb Cortex. 1–15.

Keuken MC, Forstmann BU. 2015. A probabilistic atlas of the basal ganglia using 7 T MRI. Data Br. 4:577–582.

Krauth A, Blanc R, Poveda A, Jeanmonod D, Morel A, Székely G. 2010. A mean three-dimensional atlas of the human thalamus: Generation from multiple histological data. Neuroimage. 49:2053–2062.

Liu X, De Zwart JA, Schölvinck ML, Chang C, Ye FQ, Leopold DA, Duyn JH. 2018. Subcortical evidence for a contribution of arousal to fMRI studies of brain activity. Nat Commun. 9:1–10.

Majeed W, Magnuson M, Hasenkamp W, Schwarb H, Schumacher EH, Barsalou L, Keilholz SD. 2011. Spatiotemporal dynamics of low frequency BOLD fluctuations in rats and humans. Neuroimage. 54:1140–1150.

Mitra A, Snyder AZ, Blazey T, Marcus E. 2015. Lag threads organize the brain's intrinsic

activity. Proc Natl Acad Sci. 112:E2235–E2244.

Tong Y, Lindsey KP, Hocke LM, Vitaliano G, Mintzopoulos D, Frederick BD. 2017. Perfusion information extracted from resting state functional magnetic resonance imaging. J Cereb Blood Flow Metab. 37:564–576.

Van Essen DC, Glasser MF. 2018. Parcellating Cerebral Cortex: How Invasive Animal Studies Inform Noninvasive Mapmaking in Humans. Neuron. 99:640–663.